

Jan 27th, 2026

A Low-Cost, Water-Cooled Actuator
ENGN-453

Hung-Yu Tsai (Henry Tsai)

Horace Mann School Upper Division, Bronx, New York, USA

Abstract

Quasi-direct-drive (QDD) actuators are essential for dynamic legged robots. However, commercial units remain prohibitively expensive for hobbyists, typically costing between \$150 and \$500. While 3D-printed alternatives exist, their utility is primarily limited by low continuous torque. This project introduces a 3D-printed, water-cooled QDD actuator designed to deliver metal-class continuous torque at a material cost below \$40 (excluding controller and pump).

The actuator integrates a custom BLDC motor, a 7.2:1 cycloidal planetary gearbox, and flattened copper cooling channels clamped directly to stator windings to maximize heat extraction. Structural, magnetic, thermal, and gearbox components were iteratively refined through simulation and experimental testing. The final gearbox achieved an average efficiency of 88.9%.

Active water cooling increased continuous torque from 2.1 Nm to 8.6 Nm (a 309% improvement) and raised continuous current capability from 0.85 A to 6.5 A (a 665% improvement) while keeping winding temperatures below 70°C. Peak torque reached 16 Nm at 46.5 A, approaching the performance of similarly sized metal actuators, while the 8.6 Nm continuous torque rating achieved parity with commercial QDDs.

By achieving high continuous torque using 3D-printed structural components and low-cost materials, this study demonstrates that active cooling can overcome the thermal limitations inherent in printed actuators. These results provide a practical pathway toward affordable, high-performance robotics for education and research, significantly lowering the barrier to advanced legged robot development.

1. Introduction

With the continued development of dynamic legged robots, high-torque, proprioceptive actuators have become an industry standard. The primary example, quasi-direct drive (QDD) actuators, provide the low mechanical impedance and high torque-density required for agile locomotion [1]. However, high-performance robotic actuators remain expensive and inaccessible to hobbyists despite major advances in low-cost motor controllers such as ODrive [2], Moteus [3], and the MIT Mini Cheetah controller [4]. The mechanical side of actuator design—gear reductions, motors, and thermal systems—continues to cost \$150–\$500 [5]–[8], limiting wider engagement, experimentation, and innovation.

Although recent work has begun exploring 3D-printed actuator designs, these efforts have left several important gaps unaddressed. [9] demonstrated a 3D-printed QDD actuator with a 7.5:1 reduction, achieving 19.1 Nm peak torque, but its cost remained around \$200 and its continuous torque performance was limited to 4.4 Nm. While achieving high peak torque, its continuous torque remained low when compared to metal QDD actuators such as the MIT Mini Cheetah Actuator with 6.9 Nm of continuous torque [4]. Kraft [5] and Twersky [6] further explored low-cost printed outrunner actuators, with peak torques of 29.8 Nm and 11 Nm respectively at a cost of ~\$40 without motor controllers. However, importantly, both designs lacked documented continuous torque measurements, and Twersky’s gearbox omitted bearings on the planet carrier [6], likely reducing efficiency and torque transmission.

One of the downsides of quasi-direct drive actuators which is only more prominent in 3D-printed versions is excessive joule heating. Joule heating—the heat produced by electric current passed through a motor—increases with current. At the torque needed for dynamic movements such as legged locomotion, high current is needed, creating excessive heat [1].

Without a good way to dissipate the heat produced by the actuators, these robots can often only run for limited amounts of time. For metal actuators, their aluminum casing and parts act as a heat sink, allowing for operation at high current—even if operation time may be limited. Plastics—such as the polycarbonate used by [5] and [6]—with their drastically lower thermal conductivity [10], suffer much more from joule heating in comparison to traditional metal actuators.

However, the custom machined aluminum parts which are often used in traditional actuators quickly drive up costs. Another heat dissipation method—active water cooling—represents one of the most effective ways to increase continuous performance. [1] demonstrated the feasibility of a water-cooled metal actuator, observing a 169% increase in continuous torque and a performance increase across a whole robot with multiple actuators. However, little work has been done in exploring water-cooled 3D-printed designs.

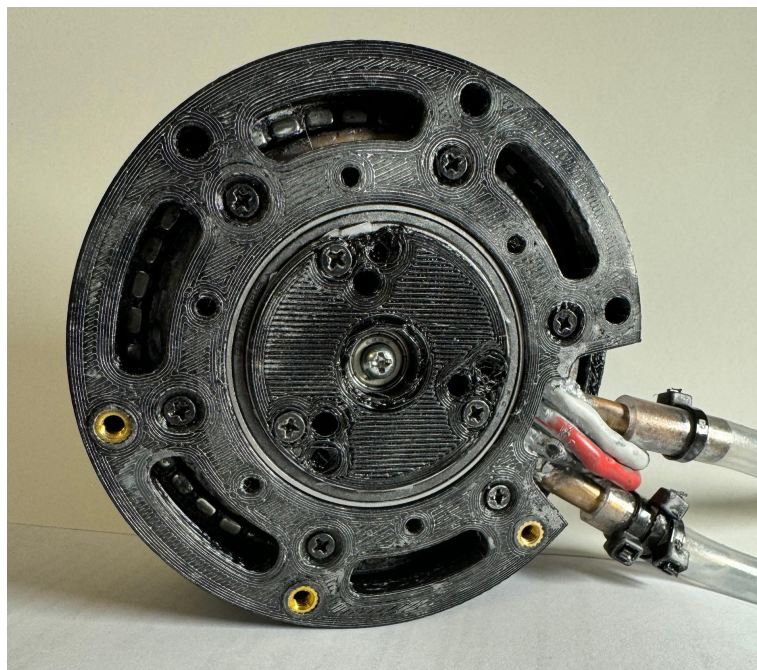
This study addresses the previously-outlined problems by integrating an active water-cooling system into a fully 3D-printed actuator, maximizing torque. The goal was to create a low-cost actuator whose continuous torque performance could reach that of metal actuators. Subgoals of reaching 14 Nm of peak torque and 7 Nm of continuous torque were set. Additionally, the hypothesis was that integrating a water-cooling loop directly in contact with the motor coils would increase continuous torque by at least 150% relative to passive cooling by removing heat more effectively.

The actuator was designed to be cheap—less than \$40 without the motor controller. It consists of 3D-printed polycarbonate parts alongside a custom BLDC motor and a single stage cycloidal planetary gearbox. Flattened copper tubing acted as the water channel, while the water

running inside transferred the heat produced by the motor to a cheap, off-the-shelf aluminum radiator through a small DC water pump.

2. Actuator Design

The actuator was mainly inspired by [4]. It was designed in Fusion 360 with over 30 static stress, structural buckling, and thermal simulations alongside over 20 part iterations. All structural points of the actuator were designed with regards to the qualities of 3D-printed polycarbonate, from shearing along layer lines to deformations in parts. The bearing configuration and motor design was calculated to sustain predicted loads and the thermal design of the actuator was optimized through simulations. The actuator was made in a home workshop and all custom parts were 3D-printed using polycarbonate filament to sustain high operating temperatures.



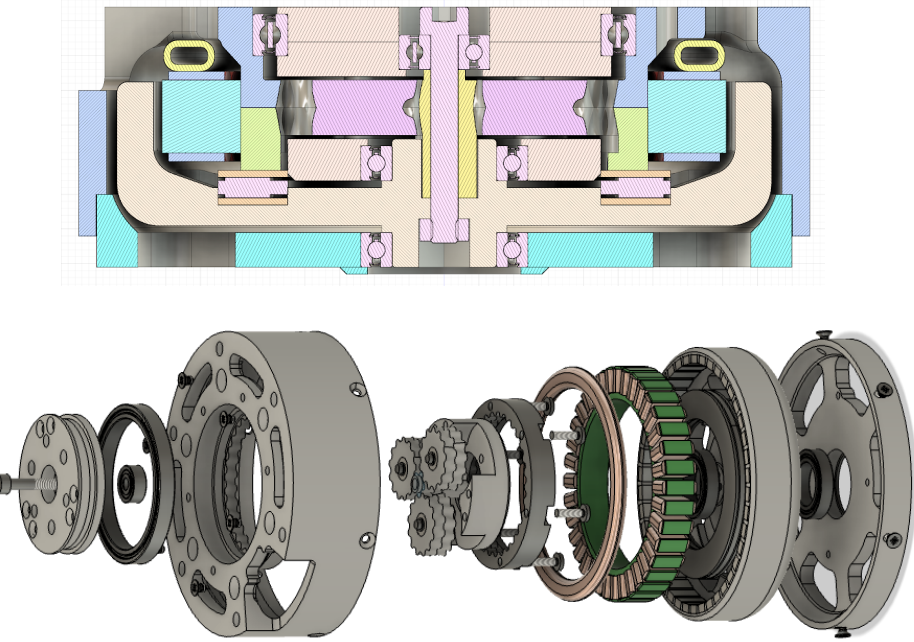
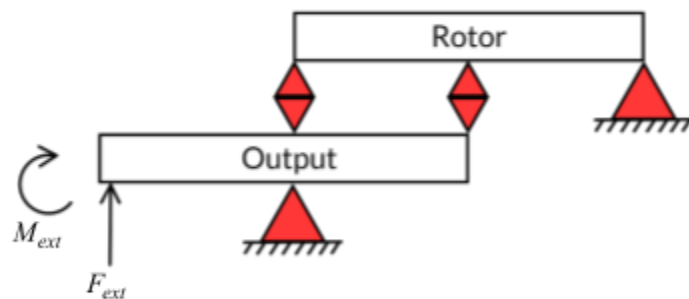


Fig. 1. Images taken by the researcher of the water-cooled actuator, its cross-section, and its components in an exploded form.

2.1 Bearings

To support robot limbs without additional external structure, the actuator must withstand significant moment loads. Following [4], a four-bearing arrangement was selected to distribute loads efficiently while maintaining compactness and low cost. The distribution of forces and moments across the bearing set was modeled by treating the actuator components as rigid bodies. The diagram below illustrates the forces at each bearing based on the specific geometry of this actuator:



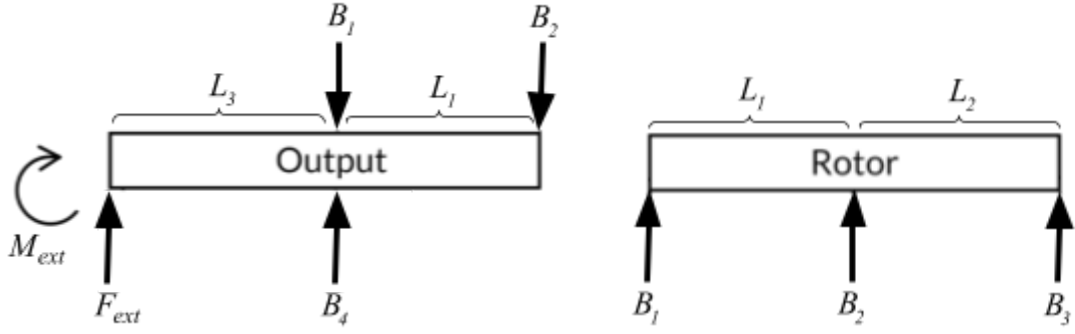


Fig. 2. Statics model of bearing arrangement, adapted from Katz [4]. Diagrams created by the researcher using Google Drawings.

By applying the principles of static equilibrium, summing the forces and moments to zero, the resulting system of equations from [4] can be solved using this actuator's specific dimensions.

The following equations describe the forces on the rotor:

$$\sum F = 0 = B_1 + B_2 + B_3 \quad (1.1)$$

$$\sum M = 0 = B_1 L_1 - B_3 L_2 \quad (1.2)$$

And for the planet carrier (output):

$$\sum F = 0 = F_{ext} - B_1 - B_2 + B_4 \quad (1.3)$$

$$\sum M = 0 = M_{ext} + F_{ext} L_3 + B_2 L_1 \quad (1.4)$$

Where $L_1 = 13.5\text{mm}$, $L_2 = 10\text{mm}$, and $L_3 = 0\text{mm}$. The required bearing loads (in Newtons) are then denoted by the vector x :

$$x = \begin{bmatrix} 31.521M_{ext} & 74.074M_{ext} & 42.553M_{ext} & 42.553M_{ext} \end{bmatrix} \quad (1.5)$$

Where M_{ext} is the external moment load applied on the actuator. The respective dynamic load ratings of the bearings—in newtons—are denoted by B_{max} , where the bearings used are 624-ZZ, 6702-2RS, 6702-2RS, and 6709-2RS bearings respectively:

$$B_{\text{max}} = \begin{bmatrix} & \\ 1300 & 940 & 940 & 2580 \end{bmatrix} \quad (2)$$

Solving for the maximum M_{ext} for all 4 bearings, the maximum moment load that each bearing can handle, in Newton-meters, can be deduced:

$$M_{\text{limit}} = \begin{bmatrix} & \\ 41.242 & 12.690 & 22.090 & 60.630 \end{bmatrix} \quad (3)$$

Thus, just like in Katz's calculations [4], the failure point lies in a 6702-2RS bearing, which limits the moment load to 12.690 Nm—lower than the actuator's desired peak torque of above 14 Nm. By changing the 6702 bearings to 6802-2RS bearings, which have dynamic load ratings of 2100 Newtons, the moment load capacity of the actuator can be increased to 28 Nm:

$$M_{\text{limit}} = \begin{bmatrix} & \\ 41.242 & 28.350 & 49.350 & 60.630 \end{bmatrix} \quad (4)$$

The resulting load capacity comfortably exceeds the actuator's peak torque requirement.

2.2 Gearbox

A cycloidal planetary gearbox was integrated within the motor stator to multiply output torque. Because 3D-printed spur gears typically fail due to thin teeth and high stress concentration, [5]'s cycloidal gear generator was used to produce gears with broader, curved teeth that distribute forces more effectively. A herringbone profile further increased load capacity. To avoid repetitive tooth pairings—which accelerate wear—coprime tooth counts of 7 (sun), 13 (planet), and 31 (ring) were selected, generating a 7.2:1 reduction.

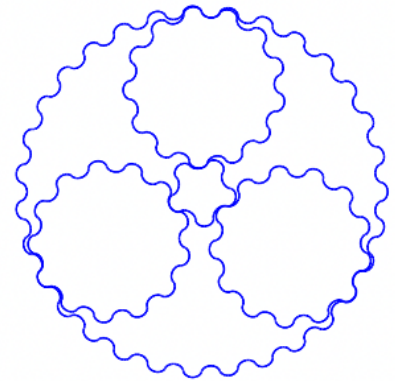


Fig. 3. An image taken by the researcher of an animation of the planetary gearbox.

Due to space constraints, the sun gear was required to be especially small. Since 3D-printed parts are weakest along the printing axis, an M4 screw was preloaded through the sun gear to enhance rigidity.

The first gearbox iteration used 693 bearings mounted on steel dowels. This design achieved a low average gearbox efficiency of 81%. The gearbox was redesigned to use three 624 bearings which provided sufficient load capacity for the low-speed operation typical of robotics actuators. A final gear backlash of 0.15mm was specified—an 0.05mm increase from before. No failures were observed after this redesign and the updated gearbox achieved 91% efficiency at peak torque while maintaining an average efficiency of 88.9%.

2.3 Motor design

The design of the custom motor was heavily influenced by [4]–[6]. To maximize torque while retaining a compact form factor, the relationship between dimensions and output was considered [11, Fig. 1.8]:

$$T = kD^2L \quad (5)$$

Where T is the torque of the motor, k the design-dependent constant, D the motor diameter, and L the length of the motor. Thus, it can be seen that the motor's torque primarily scales with its diameter with a quadratic relationship. We can further maximize torque by optimizing torque per unit rotor volume [11, Fig. 4.42]:

$$K_{\text{TRV}} = \frac{|T|}{\pi R_{r0}^2 L_{\text{st}}} = \frac{2N_m B_g N i}{\pi R_{r0}} \quad (6)$$

Thus, it can be seen that the torque per unit rotor volume, K_{TRV} , is directly proportional to the air gap radius R_{r0} , air gap flux density B_g , number of magnet poles N_m , coil turns N , and coil current i . If the stator volume and $N i$ are both constant, the torque per unit rotor volume becomes dependent on N_m and B_g . The air gap flux density B_g can be increased by decreasing the air gap length or increasing the quality or quantity of the magnets, while the number of magnet poles depends on the motor stator chosen.

Based on these factors, an 8110 36-slot stator was chosen for the motor. This rotor maximized stator diameter and the air gap radius while maintaining a sleek profile. 21 magnet poles pairs were used in the rotor; 42 10x5x3mm N52 Neodymium magnets were used. The final design had a 1mm air gap as a compromise between performance and manufacturability. Each stator slot was hand-wound with six parallel strands of AWG27 wire, yielding six turns per slot. Parallel strands increased copper fill and distributed high current across multiple conductors. Phase resistance was measured at 0.4Ω . The magnets were bonded to the polycarbonate rotor using epoxy. Large chamfers and fillets improved rotor rigidity.

The motor omits a metal back iron due to cost and machining constraints. While back iron increases usable magnetic flux and torque, including one would have greatly increased the actuator's cost. Simulations conducted using Simscale's electromagnetic analysis estimated that torque would increase by approximately 13% with a back iron.

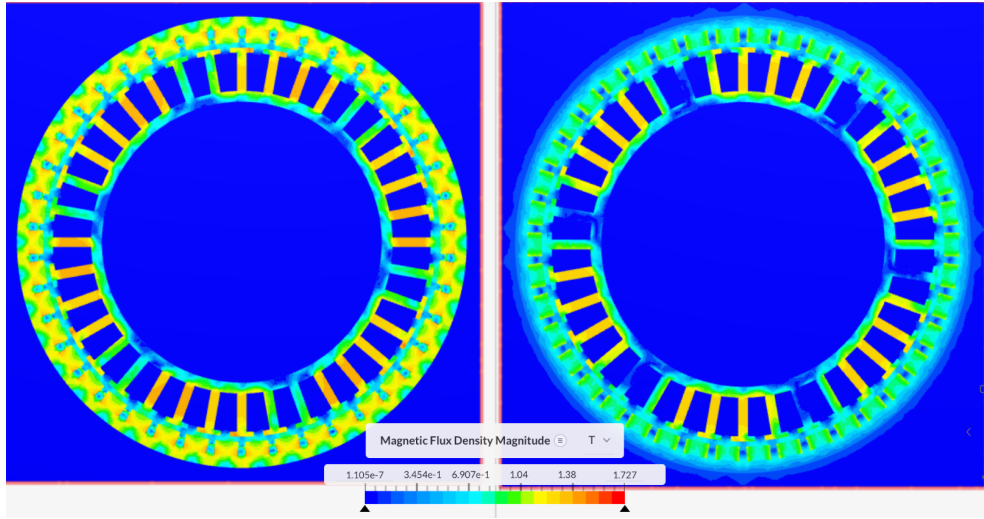


Fig. 4. Electromagnetic simulations of the motor created by the researcher using Simscale. The motor with a back iron (on the left) has significantly higher air gap flux density compared to the motor with a plastic rotor (on the right).

Originally, the rotor was designed with a 0.5 mm air gap, but rotor flex caused magnetic attraction to pull the rotor into contact with the stator. Simulations showed that the primary deformation occurred between the bearing seats and rotor body.

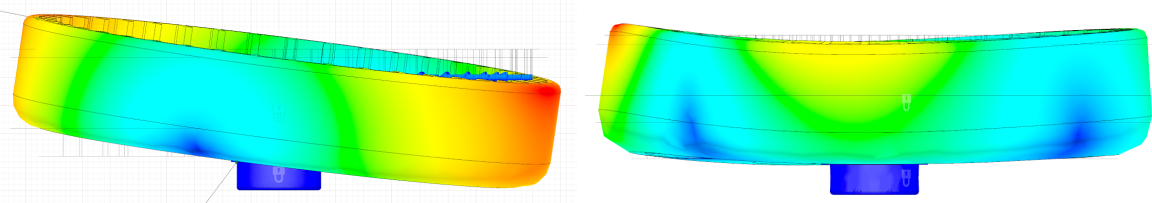


Fig. 5. Structural buckling analyses of the rotor created by the researcher in Fusion 360. The rotor with an axial bearing (on the right) had significantly less deformation than the original rotor without the added bearing (on the left).

Thus, an AXK4565 axial thrust roller bearing was placed between the rotor and the planetary gearbox's ring gear, achieving a 1 mm air gap with an 0.2 mm air gap variance.

2.4 Thermal design

To create the water channel for the active cooling system, copper tubing was selected as the primary material. Space and material constraints rendered a channel on the interior of the stator impossible. The final design placed the copper tubing directly in contact with the stator windings.

Multiple tubing geometries were simulated in Fusion 360. Flattened $\frac{1}{4}$ " copper tubing was selected for optimal thermal performance and manufacturability. Due to air gaps inherent in hand-wound coils, thermal paste was applied between the coils and tubing. Screws in the actuator housing clamped the tubing tightly onto the coils. Simulations confirmed effective heat transfer for coil-to-tubing gaps under 1 mm.

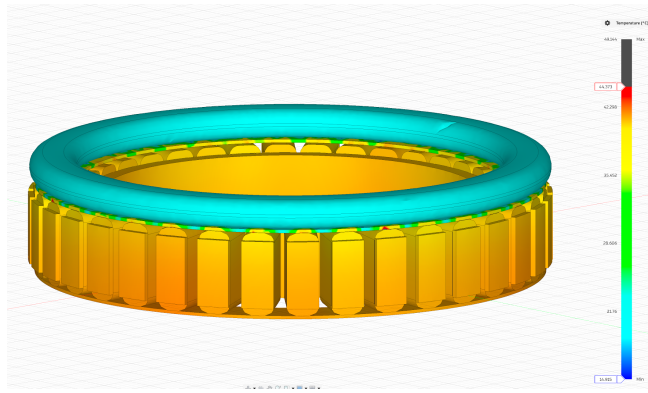


Fig. 6. A thermal analysis created by the researcher using Fusion 360 of the water-cooled actuator at 9 A of continuous current. Motor coils were modeled as solid copper blocks without accounting for enamel nor air gaps between wires, leading to lower simulated equilibrium temperatures.

During fabrication, $\frac{1}{4}$ " tubing with $13/64$ " internal diameter was bent around a 65 mm mandrel. Two rectangular inlet/outlet ports were cut, and the tubing was hammered to an 8×4

mm cross-section with ~1 mm bottom deviation. Additional copper segments were soldered for an inlet and outlet.



Fig. 7. An image taken by the researcher of the copper water channel in its position above the motor windings.

A 12 V BLDC water pump circulated distilled water from a reservoir through the actuator. Then, the heated water was passed through a dual-fan 240 mm, 12-pipe aluminum radiator before returning to the reservoir. Standard silicone tubing connected all components.

3. Testing

The actuator was mounted to a v-slot aluminum extrusion frame and a 300 mm lever arm was attached to the actuator's output. The lever was made from aluminum extrusion and balanced with additional weights. A 20 kg load cell was aligned parallel to the lever arm. The load cell output was connected through an HX711 amplifier module and read by an Arduino Uno R4.

Electrical safety procedures followed manufacturer guidelines and standard laboratory electronics safety practices. Both Moteus r4.11 and MKS XDrive V1.0 motor controllers were used, operating in field-oriented control (FOC) mode. The Moteus controller communicated through an FD-CAN adapter and the Moteus GUI, while the XDrive was controlled using ODriveTool v0.5.1. Both ran from a 12 V, 50 A power supply with an external ammeter. Internal current sensors in the controllers were logged. A thermal camera monitored actuator temperature, and continuous torque tests were halted when any part of the motor windings exceeded 70°C. Peak torque tests were held for 3 seconds. No visible damage was observed throughout testing. A Python script controlled the actuator to push against the load cell in 0.1 A increments up to 50 A while recording torque and sensor data. Torque, in Newton-meters, was computed from the measured force, in Newtons, and the length of the lever arm (0.3 m):

$$\tau = F \cdot L \quad (7)$$

4. Results

The 3D-printed water-cooled actuator achieved 8.6 Nm of continuous torque at a continuous current of 6.5 A. In comparison, the same actuator without water cooling only achieved a continuous torque of 2.1 Nm with a continuous current of 0.85 A at a similar equilibrium temperature below 70°C. Overall, this marked a 309% increase in continuous torque and a 665% increase in continuous current between the uncooled and water-cooled actuators. Both actuator setups reached a peak torque of 16 Nm at 46.5 A. The actuators were not tested at higher currents.

TABLE I
ACTUATOR SPECIFICATIONS*

Material Cost (USD)	\$37.30
Peak torque (Nm)	16 Nm
Peak current (A)	≥ 46.5 A
Continuous torque water-cooled (Nm)	8.6 Nm
Continuous current water-cooled (A)	6.5 A
Continuous torque no cooling (Nm)	2.1 Nm
Continuous current no cooling (A)	0.85 A
Gear Reduction	7.2
Weight (g)	588 g

* Table created by the researcher using Google Docs.

During testing, the actuator experienced magnetic saturation above 10 A while creating a staircase-like torque pattern:

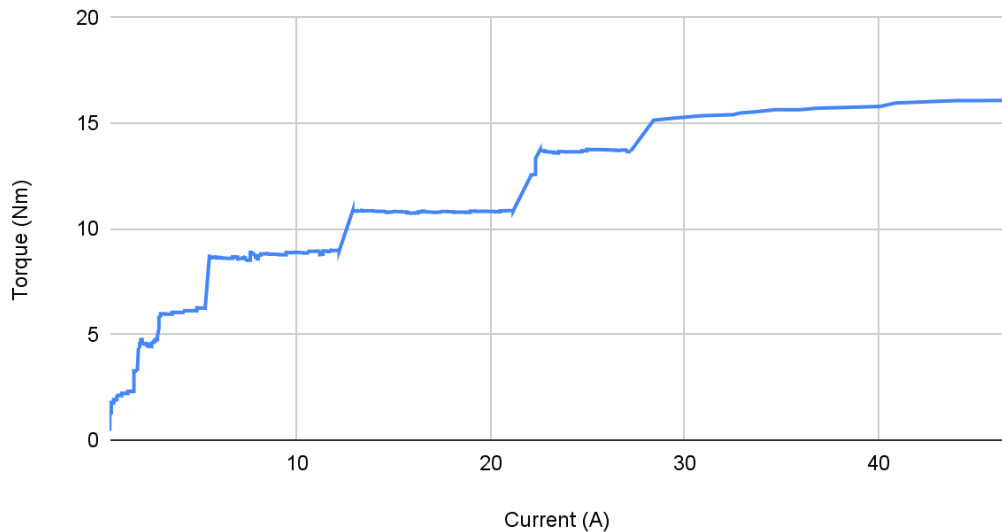


Fig. 8. The torque curve of the water-cooled actuator, relating torque to current. Graph created by the researcher using Google Sheets.

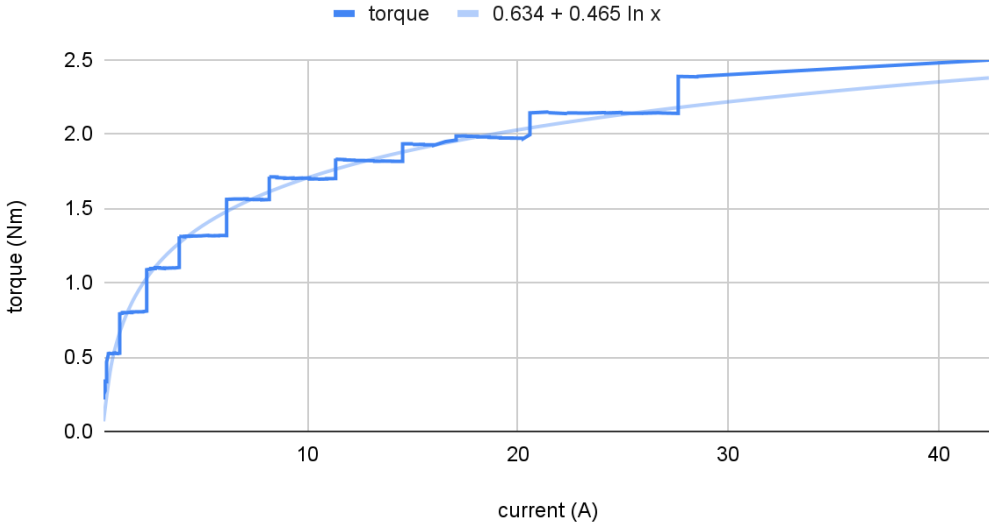


Fig. 9. The torque curve of the custom motor, relating torque to current. The rotor was directly connected to the actuator's output, bypassing the transmission. Graph created by the researcher using Google Sheets.

Without the gearbox, the motor produced 2.46 Nm of peak torque and 1.6 Nm of continuous torque at 6.5 A. Due to fixture compliance causing step-like torque curves, the gearbox efficiency was calculated from the initial torque rise in each step, yielding 88.9% average efficiency.

Water Cooling 6.5 A - Temperature to Time

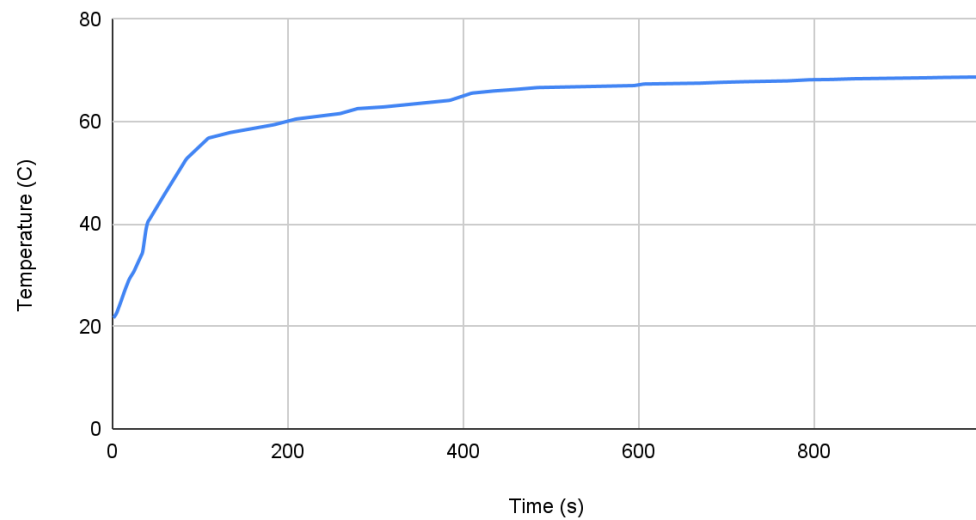


Fig. 10. Maximum motor winding temperature in a 6.5 A step with water cooling. The actuator reached thermal equilibrium just shy of 70°C. Graph created by the researcher using Google Sheets.

The water-cooled actuator was able to handle much more continuous current than the non-cooled configuration, but at currents above 30 A, the difference between the two became minimal. Both actuators often reached the set limits of 70°C within 7 seconds. At peak current, both actuators reached 70°C within 4 seconds.

No Cooling 1.1 A - Temperature to Time

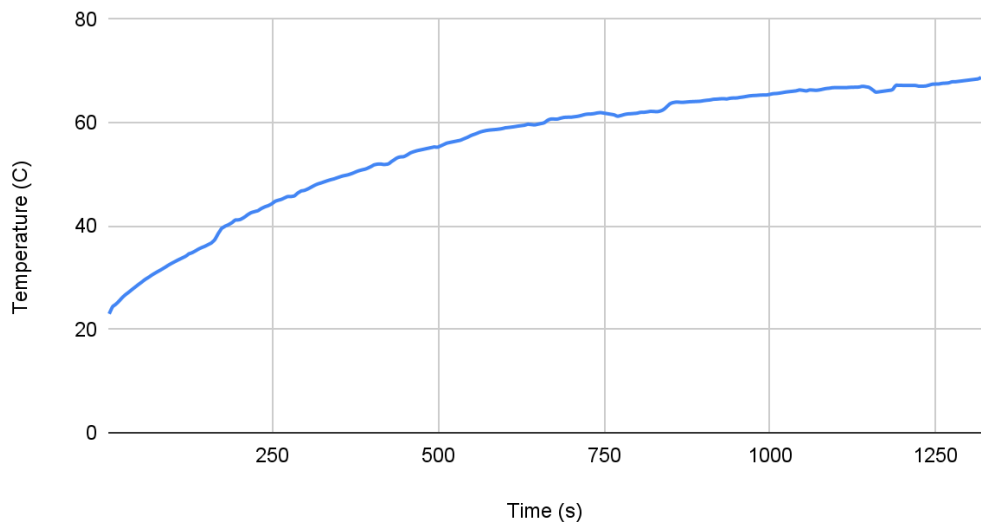


Fig. 11. Maximum motor winding temperature in a 1.1 A step without active cooling. The non-cooled actuator, past its 0.85 A continuous current, reached 70°C without stopping. Graph created by the researcher using Google Sheets.

5. Discussion

The water-cooled actuator exceeded original engineering goals, achieving 16 Nm of peak torque and 8.6 Nm of continuous torque, surpassing the original goal of 14 Nm and 7 Nm respectively. In doing so, the actuator was able to reach continuous torque performance comparable to professional metal actuators. The hypothesis was also strongly supported by the actuator's 309% improvement in continuous torque with active water-cooling which far exceeded the originally predicted 150% increase.

TABLE II
KEY ACTUATOR METRIC COMPARISON*

Key Metric	Water-Cooled (This work)	Urs. et al. [9]	MIT Mini Cheetah Actuator [4]	CubeMars AK80-9 [8]	Steadywin GIM8108-8 [7]
Transmission Ratio	7.2:1	7.5:1	6:1	9:1	8:1
Mass (g)	588	482	480	490	378
Peak Torque (Nm)	16	19.1	17	22	22
Continuous Torque (Nm)	8.6	4.4	6.9	9	7.5

* Table created by the researcher using Google Docs.

As evidenced by the comparison, the water-cooled actuator's continuous torque of 8.6 Nm proves that low-cost, 3D-printed designs can reach—and in some cases exceed—the nominal performance of similarly sized metal commercial units. While water cooling results in higher mass (588g), the trade-off is a 95% increase in continuous torque over existing printed designs like [9]. The results are consistent with the performance trends observed in water-cooled metal actuators in [1].

Since continuous torque is the primary limiting factor for a robot's payload capacity and duty cycle, these results position the actuator as a viable candidate for 10 kg-class legged robots. At a material cost of approximately \$38 per unit (excluding controller), this design offers a pathway to drastically reduce the financial barrier to high-performance robotics without sacrificing nominal power.

Admittedly, the peak torque of 16 Nm remains lower than [5]'s 29.5 Nm or the 22 Nm seen in industrial units like the CubeMars AK80-9 [8]. [5]'s performance advantage can be attributed to a larger stator and a Halbach array—features that increase complexity and cost. Similarly, the slight deficit in peak torque compared to [8] and [9] is likely a result of the magnetic saturation observed during testing. Nevertheless, the water-cooled actuator's superior

continuous torque gains significantly increase its feasibility for real-world dynamic applications where sustained power is more critical than instantaneous peak bursts.

The nonlinear torque–current relationship observed during testing suggests early magnetic saturation beginning at approximately 10 A. In an ideal BLDC motor, torque should scale linearly with current [11, p. 110]. However, the observed logarithmic behavior indicates that the magnetic flux carrying capacity of the stator was reached prematurely. This saturation is a primary reason why the actuator’s peak torque of 16 Nm remains lower than the 22 Nm achieved by professional metal actuators like the CubeMars [8] or Steadywin [7] units. As noted in Section 2.3, air-gap length and magnetic flux density have a great effect on torque. The actuator’s 1 mm air gap provides significant room for improvement through tighter manufacturing tolerances. Furthermore, the lack of a metal back iron—omitted to maintain low cost and weight—limits the peak magnetic flux density. This bottleneck becomes increasingly evident at high currents, where the plastic rotor’s inability to focus the magnetic field leads to the observed premature saturation.

The staircase-shaped torque curve may have reflected fixture or gearbox deformation: each step corresponded to slight rotor motion into a new magnetic equilibrium. The effect was more pronounced for the geared actuator which operated at higher torques. The standalone motor’s smoother curve, despite minor stepping, suggests remaining issues with air-gap uniformity and fixture stiffness. Even after multiple redesigns, a high air-gap variation of 0.2 mm (20%) was measured, which likely contributed to the irregular curve. This air-gap variation was caused by rotor misalignment due to the lower accuracy of FDM 3D-printing which multiplied over several connected components.

According to electromagnetic and structural simulations, addressing these manufacturing variances is the clear next step for performance parity. Tightening air-gap tolerances through post-process machining or higher-resolution printing, combined with reinforced structural ribs to increase rigidity, would likely allow the actuator to better compete with the peak torque ratings of industrial metal actuators while maintaining its significant cost advantage.

6. Conclusion

The water-cooled 3D-printed actuator exceeded expectations, achieving a threefold increase in continuous torque and demonstrating reliable, repeatable operation. While numerous design and manufacturing issues arose, each major fault was successfully resolved. The degree of magnetic saturation observed was unexpected, but simulations point toward feasible improvements for future iterations.

Although the weight and water-cooling logistics of implementing such an actuator into complete robots still necessitates future experimentation, its high torque may still enable the possibility of significantly cheaper dynamic legged robots. This increased accessibility could benefit hobbyists, educational programs, and small research groups who are currently limited by actuator cost. Since proprioceptive actuators such as this one are central to state-of-the-art robotics, improved affordability may substantially broaden participation in advanced robotics research and development.

References

- [1] T. Zhu, J. Hooks and D. Hong, "Design, Modeling, and Analysis of a Liquid Cooled Proprioceptive Actuator for Legged Robots," *2019 IEEE/ASME International Conference on Advanced Intelligent Mechatronics (AIM)*, Hong Kong, China, 2019, pp. 36-43, doi: 10.1109/AIM.2019.8868596.
- [2] "ODrive S1," *ODrive Robotics*. [Online]. Available: <https://shop.odriverobotics.com/products/odrive-s1> (accessed Sep. 10, 2025).
- [3] "Moteus r4.11," *mjBots Robotic Systems*. [Online]. Available: <https://mjbots.com/products/moteus-r4-11> (accessed Sep. 10, 2025).
- [4] B. G. Katz, "*A low cost modular actuator for dynamic robots*," M.S. thesis, Dept. Mech. Eng., Massachusetts Institute of Technology, Cambridge, MA, USA, 2018. [Online]. Available: <https://dspace.mit.edu/handle/1721.1/118671>.
- [5] C. Kraft, "Ironless Rotor Cycloidal Planetary Actuator," *Caden Kraft*, Jul. 12, 2025. [Online]. Available: <https://cadenkraft.com/ironless-cycloidal-planetary-actuator/> (accessed Aug. 30, 2025).
- [6] N. Twersky, "3D Printed QDD Robotic Actuator (MIT Mini Cheetah Clone)," *Instructables*, Jan. 13, 2025. [Online]. Available: <https://www.instructables.com/3D-Printed-QDD-Robotic-Actuator-MIT-Mini-Cheetah-C/> (accessed Aug. 27, 2025).
- [7] "GIM8108-8 planetary reduction motor robot dog humanoid robot joint module flat thin large torque," *Steadywin*. [Online]. Available: <https://steadywin-motor.com/products/planetary-reduction-motor-robot-dog-humanoid-robot-joint-module-flat-thin-large-torque> (accessed Nov. 29, 2025).
- [8] "AK80-9 V3.0 Robotic Actuator," *CubeMars*. [Online]. Available: <https://www.cubemars.com/product/ak80-9-v3-0-robotic-actuator.html> (accessed Dec. 20, 2025).
- [9] K. Urs, C. E. Adu, E. J. Rouse and T. Y. Moore, "Design and Characterization of 3D Printed, Open-Source Actuators for Legged Locomotion," *2022 IEEE/RSJ International Conference on Intelligent Robots and Systems (IROS)*, Kyoto, Japan, 2022, pp. 1957-1964, doi: 10.1109/IROS47612.2022.9981940.

- [10] “Plastic Thermal Conductivity Reference Table,” *Alfa Chemistry*, 2018. [Online]. Available:
<https://www.alfa-chemistry.com/plastics/resources/plastic-thermal-conductivity-reference-table.html> (accessed Sep. 3, 2025).
- [11] D. Hanselman, *Brushless Permanent Magnet Motor Design*, 2nd ed. Lebanon, Ohio, USA: Magna Physics Pub, 2006. [Online]. Available:
<https://blog.avilab.com/uploads/2014/05/BrushlessPermanentMotorDesignVersion2.pdf>. Accessed: Sep. 7, 2025.